



<https://doi.org/10.15407/ufm.24.01.075>

O.M. IVASISHIN^{1,*}, D.V. KOVALCHUK², P.E. MARKOVSKY^{1,},
D.G. SAVVAKIN^{1,***}, O.O. STASIUK¹, V.I. BONDARCHUK¹,
D.V. ORYSHYCH¹, S.G. SEDOV³, and V.A. GOLUB³**

¹ G.V. Kurdyumov Institute for Metal Physics,
36, Academician Vernadsky Blvd., UA-03142 Kyiv, Ukraine

² JSC 'NVO 'Chervona Khvylya',
28 Dubrovytska Str., UA-04114 Kyiv, Ukraine,

³ National University of Defense of Ukraine named after Ivan Cherniakhovskiy,
28 Povitroflotsky Ave., UA-03049 Kyiv, Ukraine

* ivas@imp.kiev.ua, ** pmark@imp.kiev.ua, *** savva@imp.kiev.ua

ADDITIVE MANUFACTURING OF TITANIUM-BASED MATERIALS USING ELECTRON BEAM WIRE 3D PRINTING APPROACH: PECULIARITIES, ADVANTAGES, AND PROSPECTS

Potential of additive manufacturing technologies, namely, xBeam 3D Metal Printing for the fabrication of uniform Ti-6Al-4V (Ti-6-4, mas.%) material as well as layered titanium-based structures, with mechanical properties sufficient for wide practical application is demonstrated. The key distinctive features of this process are titanium alloy wire as a feedstock material and hollow conical electron beam for heating and melting of the wire. 3D printed with special 'shift strategy' Ti-6-4 alloy meets requirements to mechanical characteristics of corresponding conventional cast and wrought products, if microstructure features, material anisotropy and crystallographic texture are controlled with proper selection of processing parameters. Production of multilayered materials consisting of combined layers of different ti-

Citation: O.M. Ivasishin D.V. Kovalchuk, P.E. Markovsky, D.G. Savvakina, O.O. Stasiuk, V.I. Bondarchuk, D.V. Oryshych, S.G. Sedov, and V.A. Golub, Additive Manufacturing of Titanium-Based Materials Using Electron Beam Wire 3D Printing Approach: Peculiarities, Advantages, and Prospects, *Progress in Physics of Metals*, 24, No. 1: 75–105 (2023)

© Publisher PH "Akademperiodyka" of the NAS of Ukraine, 2023. This is an open access article under the CC BY-ND license (<https://creativecommons.org/licenses/by-nd/4.0/>)

tanium materials, *viz.* commercially pure titanium (CP-Ti), Ti-6-4 and high-strength T110 alloys, as well as metal matrix composites (MMC) based on Ti-6-4 matrix reinforced by fine TiC particles is considered. Microstructural features and mechanical properties of all 3D printed materials are investigated. Terminal ballistic tests are performed with different ammunition. Described results show the promising potential of 3D printing technologies, xBeam 3D Metal Printing as an example, for manufacturing of titanium-based multilayered armour materials with reduced thickness and weight, and at the same time, sufficient protection characteristics.

Keywords: titanium alloys, 3D printing, microstructure, multilayered material, mechanical properties, antiballistic protection.

1. Introduction

Titanium-based alloys and metal matrix composites are attractive lightweight construction materials for wide application in aerospace, automotive, chemical, defence industries, civil engineering and medicine owing to excellent strength to weight ratio and brilliant corrosion resistance [1]. However, high price of titanium itself and complex multi-stage technologies of alloy ingot melting, treatment and machining contributing the high cost of titanium-based products restrict the areas of their application. Therefore, development of new manufacturing technologies to obtain titanium products possessing high characteristic at reduced cost are the aim of a number of research efforts.

3D printing, also known as additive manufacturing (AM) [2–5], has been widely used in industry for the rapid and cost-effective production of near-net-shape polymeric articles, while attractive expansion of this approach for manufacturing of various metallic articles met significant problems at the beginning and resulted in compromised physical and mechanical characteristics. Later, the development of metal 3D printing processes became an important milestone in the AM evolution, which allowed producing titanium prototypes possessing basic properties close to those for parts manufactured with traditional cast and wrought metallurgy. Despite commonly acknowledged economy advantages of AM processing, the real industrial use of 3D printed products required full compliance of their microstructure and entire complex of physical and mechanical properties with the requirements of the relevant industry standards.

By their physical and metallurgical nature, metal 3D printing methods consist in intensive local heating of feedstock metal to form a small volume of liquid metal on substrate, its subsequent quick cooling and solidification to build the next layer of a three-dimensional product [2–5]. Therefore, the main characteristic features of the layer-by-layer AM produced metal structure are very similar to those of casting processes, including the formation of defects (pores, lack of fusion), the nuc-

leation and growth of crystals, the appearance of residual stresses due to fast localized heating and cooling, *etc.*

Important issue is achievement of sufficient and isotropic mechanical, and, hence, operational characteristics of 3D printed titanium articles. This aim can be achieved with decrease in residual stresses and reduction of material properties anisotropy arising due to the columnar grain structure elongated in the direction of product growth as well as due to lack of fusion and porosity between printed layers [2–7]. Such not optimized structures lead to variation of the mechanical properties, especially ductile characteristics, in different directions. In order to destroy the columnar grains and to form isotropic poreless metal structure similar to the structure of a wrought material, some developers used additional thermomechanical processing like rolling of each just built layer or shaped forging of the entire AM product.

Among other metallic materials, the AM technologies are also widely used for cost-efficient manufacturing of titanium-based shaped products for various applications [5, 8–10]. Ti–6Al–4V (Ti-6-4, wt.%) alloy as the most widely used titanium composition over the world is the main object of AM research and development efforts to achieve sufficient set of characteristics.

However, despite attractive combinations of strength and ductile properties, conventional titanium alloys like Ti–6Al–4V or other compositions needs further improvement of characteristics to meet requirements for some extremal loading conditions, to enhance wear resistance and to ensure confident protection against ballistic impact and penetration of projectiles in military application [11–17]. Enhanced set of strength/ductile characteristics, wear resistance and better antiballistic protection can be achieved with creation of multilayered structures, which combine layers of various titanium alloys and/or metal matrix composites (MMC) with quite different properties as entire article [14–19]. As an example, combination of high-strength hard MMC or high-strength alloy layer with lower-strength alloy having enhanced fracture toughness and ductility improves strength/ductility balance ensuring set of characteristics unattainable for each individual material. Taking in mind that 3D printing technologies have wide opportunities for variations in chemical composition of individual layers, this approach has an attractive potential for manufacturing of multilayered structures, which combine various titanium alloys and titanium MMCs, thus, providing enhanced characteristics.

The purpose of the present study was to demonstrate recent developments in achievement of acceptable microstructures and sufficient mechanical characteristics of massive Ti–6Al–4V products and titanium-based multilayered structures by 3D printing using AM approach based on advanced electron beam melting technology. The paper describes

methods for optimization of 3D printed microstructure with careful control of processing parameters and demonstrates potential to achieve high characteristics of 3D manufactured products, which are sufficient for sustainable application in aerospace and defence industries.

2. xBeam 3D Metal Printing Technology for Manufacturing of Titanium Objects: Peculiarities and Advantages

The samples for investigation were manufactured with the xBeam 3D Metal Printing method, which uses a titanium alloy wire as feedstock material and profile electron beam in the form of a hollow inverted cone to melt a wire which is fed coaxially with this electron beam [20–23]. The general process scheme is shown in Fig. 1, when melt pool is formed on a substrate during layer-by-layer printing of 3D products. Ti–6Al–4V alloy wire with a diameter of 3 mm was used as the main feedstock material, commercially pure titanium (CP-Ti) wire 3 mm in diameter was also used in some experiments.

xBeam 3D Metal Printing method as advanced additive manufacturing technology was developed by JSC ‘NVO Chervona Khvylya’ [20–23]. The unique hollow conical configuration of electron beam (Fig. 2) ensures useful and important technological features of this method, namely, opportunity for precise control of the thermal fields both in the molten zone where the melt pool is formed and additive material is deposited, and in the heat affected zone. Moreover, the use of a low-voltage electron beam, which has a high total power up to 18 kW, but creates a

moderate concentration of energy on the heating surface (in the range of 10^3 kW/cm²), provides a number of exceptional technological possibilities for manufacturing of high-quality articles with high productivity.

Moderate concentration of power on the heated surfaces prevents significant overheating of the melt and allows avoiding high temperature gradients in the surrounding volume of the metal [20]. It prevents deep melting of the previous layer (the depth of the melt pool usually does not exceed 0.5–1.0 mm) and allows achieving very high cooling rates with fast

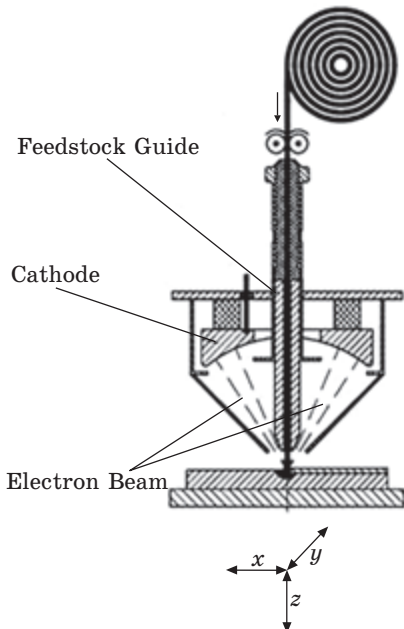
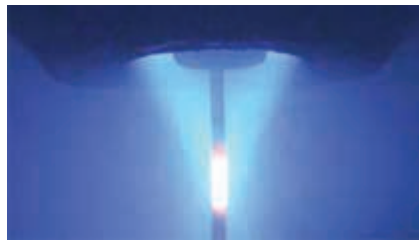


Fig. 1. General design and process configuration of the xBeam concept [20]

Fig. 2. Wire heating area by a hollow conical converging electron beam [20]



solidification. These factors provide intensive nucleation of multitude crystallization centres in the molten volume and inhibition of grain growth, thus, reduce the probability of continued grain growth from the previously crystallized layers. As a result, controllable grain structure of 3D printed material can be produced without formation of coarse columnar-like grains harmful for high mechanical characteristics of final products. In addition, low specific power input with gradual reduction of power heating intensity from the maximum to the periphery highly reduces residual stresses and distortions of the produced parts, which currently is considered as one of the critical problems of existing metal AM methods [2, 5, 8, 10, 20, 24–25].

3. Optimization of xBeam 3D Metal Printing Parameters to Achieve Desirable Material Microstructure and Characteristics

The practice application of 3D printed metal products, including titanium ones, needs sustainable achievement of their high and rather isotropic mechanical characteristics similar to those for corresponding cast and wrought materials. This aim, in turn, requires formation of controllable isotropic microstructure without undesirable defects such as lack of fusion between printed layers, pores (Fig. 3, *a*, *b*) and without weak structure elements such as large columnar-like grains (Fig. 3, *c*).

To avoid above noted microstructure defects, a number of methods for optimization of 3D printing process were developed by various researches [2–5]. JSC ‘NVO Chervona Khvylya’ made considerable efforts [20–23] aimed on structure improvement and formation of isotropic

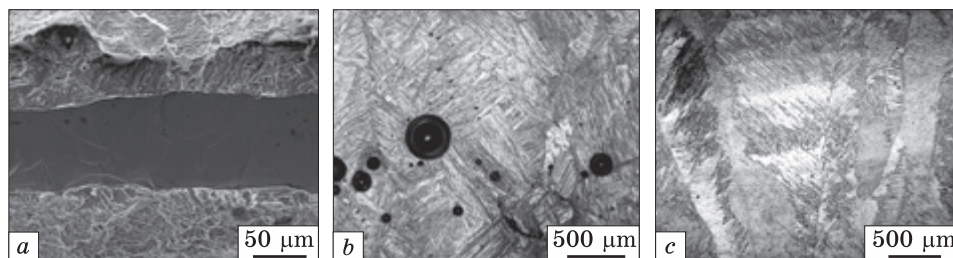


Fig. 3. Undesirable microstructural elements typically formed in 3D printed metal products, where *a* — large void due to lack of fusion between neighbouring layers, *b* — pores, and *c* — columnar-like grains. (Ti–6Al–4V alloy as an example)

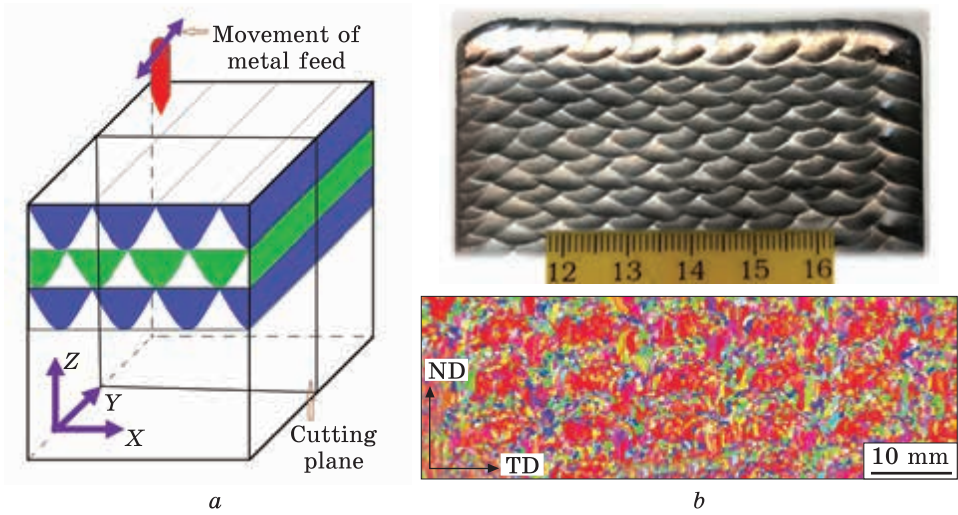


Fig. 4. Scheme (a) illustrating 'shift strategy' [26] of 3D printing, (b) general view of Ti-6Al-4V side printed surface and β -phase EBSD orientation map (reconstructed from the α -phase) of vertical cross section shown

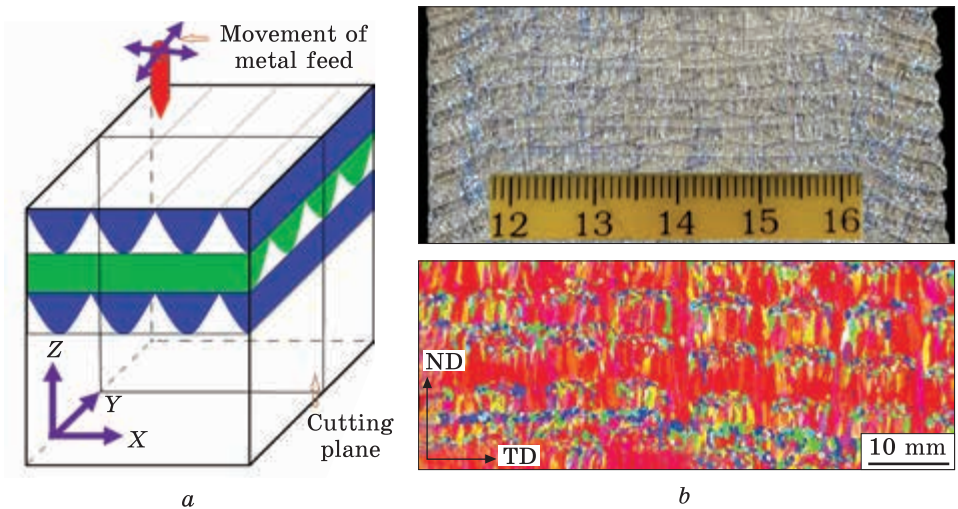
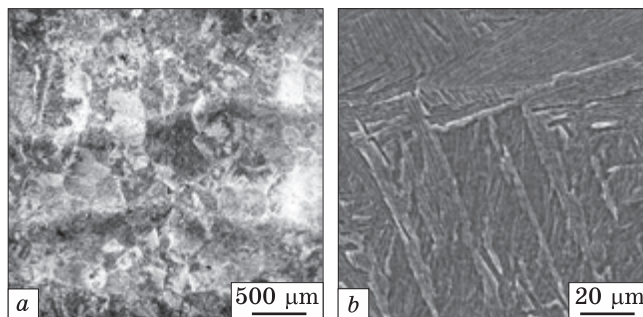


Fig. 5. Scheme (a) illustrating 'lattice strategy' [26] of 3D printing, (b) general view of Ti-6Al-4V cross section structure and β -phase EBSD orientation map (reconstructed from the α -phase) of vertical cross section shown in (a)

uniform printed titanium products, namely, two strategies [23] for optimization of 3D printing process ('shift strategy', Fig. 4 and 'lattice strategy', Fig. 5) were developed. Both methods are based on specific geometry of molten bead deposition on previously built layer. In the 'shift strategy' (Fig. 4, a) all beads were deposited on the previous layer

Fig. 6. Relatively fine grained and uniform microstructure of 3D printed Ti-6Al-4V material with visible horizontal interlayer boundaries (a) and typical fine lamellar intragrain structure (b)



in the same horizontal direction (along the X coordinate), but all beads within each subsequent layer were deposited with some shift upon the previous correspondent bead along the Y coordinate, almost in the middle between the beads of previously deposited layer. Such layers were alternated from the bottom part (substrate) and until the top of built sample, forming uniform structure without harmful defects (Fig. 4, *b*). In ‘lattice strategy’, all beads of each next layer were deposited across the direction of previously deposited layer (Fig. 5, *a*) from the bottom layer (substrate) and until the top of the built sample. This approach also is very promising to ensure the dispersed and uniform microstructure of as-built Ti-6Al-4V material (Fig. 5, *b*).

Extremely important achievement of both above described strategies is inhibition of directed grain growth through a number of adjacent 3D printed layers, thus, preventing formation of large columnar-like grains (like those presented in Fig. 3, *c*). Usually, undesirable vertically elongated grains are formed in the lower part of each layer, starting from the first one, because the cooling front is directed vertically downward the colder substrate or previous layer. In the upper part of each layer, due to the intense thermal irradiation and, hence, higher cooling rates, a much finer nearly equiaxed grain structure is formed. However, when the next layer is deposited, the melt pool is usually deep enough to reach the columnar crystals of the previous layer; their top surfaces serve as nuclei for melt crystallization leading to continuation of grain growth vertically upward. If the moulded area within next deposited layer does not reach columnar grains in previous layers, there is a high probability for nucleation of new grains. The forming of a shallow melt pool provides higher cooling rates on crystallization and lower heat influence on previous layers, thus, creating benefit conditions to form new ‘independent’ equiaxed grains and formation of an isotropic relatively fine-grained structure. So, taking into consideration discussed above, optimization of xBeam metal printing parameters such as rate of metal feeding to heating area, rate of substrate moving and specific energy concentrated in heating area allow to control melting, crystallization and cool-

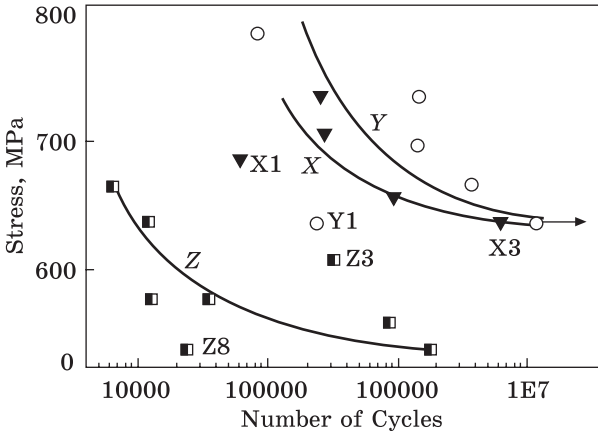


Fig. 7. Fatigue strength data for specimens manufactured in different directions of Ti-6Al-4V block 3D printed by 'shift strategy' [26]

ing conditions within 3D printing area and in heat affected zones nearby, which, in turn, ensure formation of desirable microstructure.

Both shift and lattice strategies were successfully tested for 3D printing of 'chunky' Ti-6Al-4V blocks (60×60×70 mm in size); sufficient uniformity of isotropic microstructure was achieved (Fig. 6, a). Fast cooling resulted in formation of either metastable α' -martensite intragrain structure or not completely stable fine lamellar $\alpha + \beta$ one (Fig. 6, b) [8, 9, 20, 26, 27]. Thus, post-printing annealing (heat treatment) is necessary to produce fully stable $\alpha + \beta$ structure, to reduce stresses accumulated in the material due to repeated relatively fast heating/cooling cycles, and in such a manner, to improve strength and ductility balance [20, 24, 26]. The tensile characteristics of annealed blocks were tested using samples cut in 3 reciprocally perpendicular directions (Table 1, X and Y are horizontal directions along the printed layers, while Z one is vertical across them) to evaluate material isotropy. It was demonstrated [26] sufficient uniformity of rather high tensile characteristics in horizontal directions, while some lower characteristics were achieved in vertical direction across the printed layers. The tested hardness was within 321–335 HV over the printed Ti-6Al-4V blocks, also confirming sufficient uniformity of the material. Noted tensile and hardness characteristics met standard requirements for cast and wrought Ti-6Al-4V alloy, excluding tensile elongation in vertical Z direction which was the only parameter some lower than standard requirement. It was concluded that

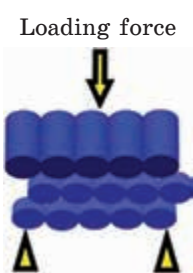
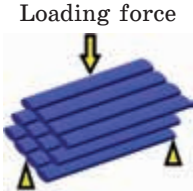
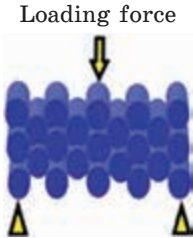
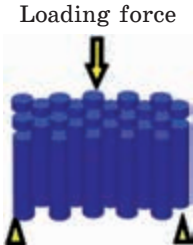
Table 1. Tensile properties of 3D-printed Ti-6Al-4V material in annealed/stress relieved condition (characteristics for 'shift strategy' are presented as an example)

Tested direction	Yield strength (YS), MPa	Ultimate tensile strength (UTS), MPa	Tensile fracture elongation (El), %	Reduction of area (RA), %
Z	928 ± 28	966 ± 25	7.2 ± 2.6	11.2 ± 3.4
X	978 ± 21	1014 ± 18	15.2 ± 2.5	26.2 ± 6.6
Y	971 ± 19	1009 ± 17	16.3 ± 2.3	28.3 ± 7.2

both printing strategies [26] can be successfully employed for 3D printing of various titanium products, and were used for manufacturing of samples for experiments described below.

Particular attention was also paid to the fatigue properties of the 3D printed material [26] from point of view of wide practical application of such material. Fatigue tests were performed with samples of the hourglass type by rotation-bending (rotating beam) method at 50 Hz frequency, at room temperature with symmetric loading cycle. Two pe-

Table 2. Results of three-point flexure tests of 3D printed Ti-6Al-4V material ('shift strategy') depending on applied load orientation to printed layers and beads

#	Loading direction (denoted by vertical arrow)		Flexure strength, MPa	Flexure strain, %
1	Perpendicular to printed layers and beads (beads are perpendicular to the sample axis)		1870	18.3
2	Perpendicular to printed layers and beads (beads are in parallel to sample axis)		1921	10.1
3	Along to printed layers and perpendicular to beads		1960	19.8
4	Along to printed layers and beads		1969	18.5

cularities of fatigue test results (Fig. 7) should be noted. First, *S-N* curves demonstrated a relatively large spread of fatigue strength values within each group of specimens (*i.e.*, for samples manufactured in the same direction). Secondly, very high fatigue strength values of the Ti-6Al-4V alloy (maximum value of 770 MPa for 'Y' group of samples) and the high fatigue limits similar for groups 'Y' and 'X' (about 630 MPa) were observed. The samples manufactured in 'Z' direction are characterized with a large scatter of fatigue strength values, which can be related to microstructure features in this direction intersecting parallel layers of as-build block. Such conclusion was confirmed by presence of printing defects at the fractured surfaces of some tested samples.

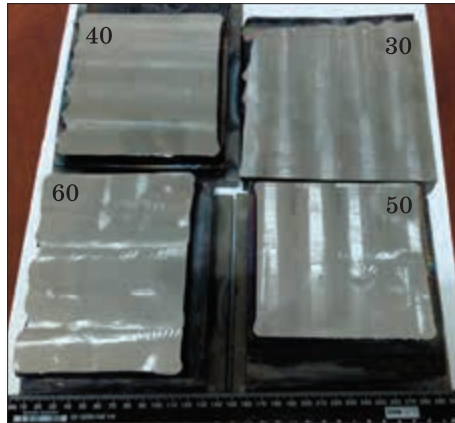
Three-point flexure tests were performed with rectangular $10 \times 10 \times 60$ mm samples cut out with spark erosion in 4 different directions from Ti-6Al-4V alloy block 3D printed *via* 'shift strategy'. Samples orientated in parallel and in perpendicular directions to printed layers and printed beads (as it is presented in Table 2) were tested to clarify material behaviour depending on direction of load applied. The results demonstrated obvious change of 3D printed material characteristics depending on loading direction. The best strength (1960–1969 MPa) and strain (18.5–19.8%) characteristics were achieved when loading force was applied along to printed layers independently on orientation of printed beads (Table 2). This result once more confirms sufficient bonding between printed layers and beads because of interfaces between layers and beads are subjected to tensile and compression stresses at such loading direction. The lowest strength (1870 MPa) without compromising of strain characteristics was achieved when load was applied perpendicularly to printed layers and beads. The intermediate strength level at worst deformation (10%) was observed at loading in perpendicular direction to printed layers when beads are in parallel to sample axis.

Summarizing all the above data, we can conclude that the application of conic xBeam wire technology for 3D printing of typical titanium alloy Ti-6Al-4V can ensure desirable balance of standard mechanical properties meeting the requirements of a wide range of practical applications. However, important attention should be paid to the effects of structural and crystallographic texture of 3D printed material, which determine some variations in properties in certain directions.

4. Characterization of 3D Printed Uniform Ti-6Al-4V Plates of Different Thickness

As the first research step to check validity of 3D printed titanium products for application as antiballistic armour elements, uniform Ti-6Al-4V plates of various thickness were printed. Plates 30, 40, 50 and 60 mm in thickness and about of 175×150 mm in plan were manufactured and

Fig. 8. General view (rear side) of 3D printed Ti-6-4 plates of different thickness prepared for ballistic tests



annealed to reduce residual stresses (Fig. 8). Backsides of all plates were machined to achieve relatively smooth surfaces and to avoid stress concentrators harmful for antiballistic resistance. Plates were subjected to ballistic tests (Fig. 9) using two kinds of B-32 armour-piercing projectiles (Table 3) differing in calibre, mass and kinetic energy. In addition, microstructures within severely deformed areas near projectile penetration channels were thoroughly investigated. The comprehensive analysis of ballistic tests (Table 3), 3-point flexure tests (Table 2) and microstructural data allows clarifying behaviour of 3D printed Ti-6Al-4V alloy under high-speed impact loading.

The projectiles of lower calibre (7.62 mm) demonstrated ability for 17–20.5 mm depth penetration in Ti-6Al-4V plates (Table 3). Therefore, even the lowest thickness of the plate (30 mm) is sufficient for sustainable antiballistic protection against the noted projectiles. The projectiles of 12.7 mm calibre, owing to noticeable higher mass and kinetic energies pierced plates 30 mm in thickness (Fig. 9, a) and even 40 mm (Fig. 9, b) with fragmentation of back side (Figs. 9, e, 10, a), while thicker plates were able to stop the 12.7 mm projectiles (Fig. 9, c, d, f) at 35–36 mm depth (Fig. 10, b). Obviously, 40 mm thickness is

able to stop the 12.7 mm projectiles (Fig. 9, c, d, f) at 35–36 mm depth (Fig. 10, b). Obviously, 40 mm thickness is

Table 3. Ballistic test results of 3D printed Ti-6Al-4V plates of different thickness

##	Plate thickness, mm	Bullet calibre*, mm	Projectile speed, m/s	Kinetic energy of projectile, kJ	Result	Penetration depth, mm
1	30	7.62	850	3.76	Not pierced,	17.0
2		12.7	861	17.90	Pierced	N/A
3	40	7.62	854	3.79	Not pierced,	20.0
4		12.7	859	17.82	Partially pierced	N/A
5	50	7.62	853	3.78	Not pierced	20.5
6		12.7	851	17.49	Not pierced	36.0
7	60	7.62	856	3.81	Not pierced	20.5
8		12.7	858	17.78	Not pierced	35.0

* Each plate was tested by two kinds of B-32 projectiles: 7.62 mm calibre, 10.4 g mass, and 12.7 mm calibre, 48.3 g mass.



Fig. 9. Front view of Ti-6Al-4V plates of different thickness (*a* — 30 mm, *b* — 40 mm, *c* — 50 mm, *d* — 60 mm) after ballistic tests. Backsides of 30 mm plate pierced with 12.7 mm projectiles (*e*) and not pierced 50 mm plate (*f*) are also shown

critical value for protection against 12.7 mm projectiles. Lower thickness cannot ensure protection due to fracture of backside of plate, while sustainable protection needs plate thickness more than 40 mm.

Influence of bullets energy on the depth of their penetration in these tests is presented on Fig. 11. Analysing these data, it is possible to conclude, that for case of 7.62 mm calibre some evident dependence of exponential character is seen (Fig. 11, *a*). The most intensive increase in penetration depth took place for bullets' energies in the range of 3750–3820 J. At the same time, it is not visible influence of tested

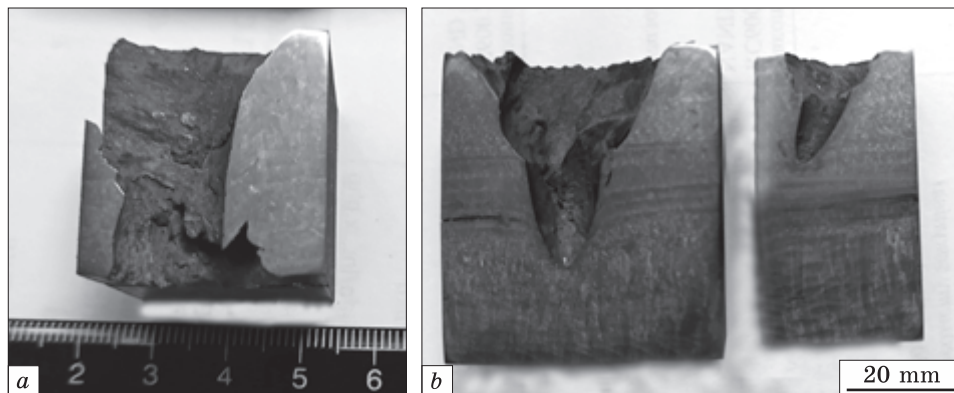


Fig. 10. Cross sections of Ti-6Al-4V plates showing projectiles penetration channels (projectile movement are in downward directions): *a* — complete piercing of 30 mm thick plate with back side fragmentation with 12.7 mm calibre bullet, *b* — projectile stopping inside the plate by different calibres

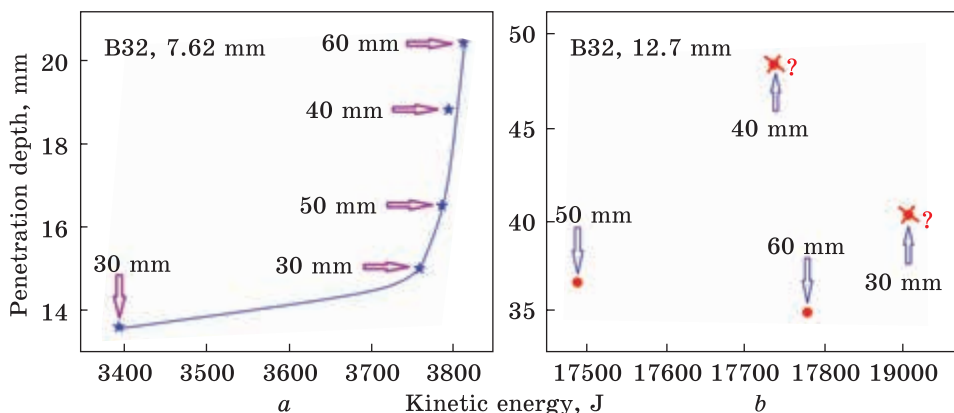


Fig. 11. Dependences between the kinetic energy of B32 bullets and depth of its penetration into the 3D printed Ti-6-4 alloy for (a) 7.62 mm and (b) 12.7 mm calibres. Thickness of plates is indicated with arrows

plates' thickness since the points on the curve shown solely as a function of the kinetic energy. Another situation is in case of shots with 12.7 mm calibre ammunition (Fig. 11, *b*), namely, no dependence of the penetration depth on either the kinetic energy or the thickness of the plates is observed. True, the number of results is clearly not enough for reliable statistics. However, some conclusions can be made, if kinetic energy (E) is recalculated into specific values, *i.e.*, relative to the plate thickness (d_1) for pierced plates or relative to the penetration depth (d_2) for non-pierced plates. In this case for plates 30 mm and 40 mm we re-

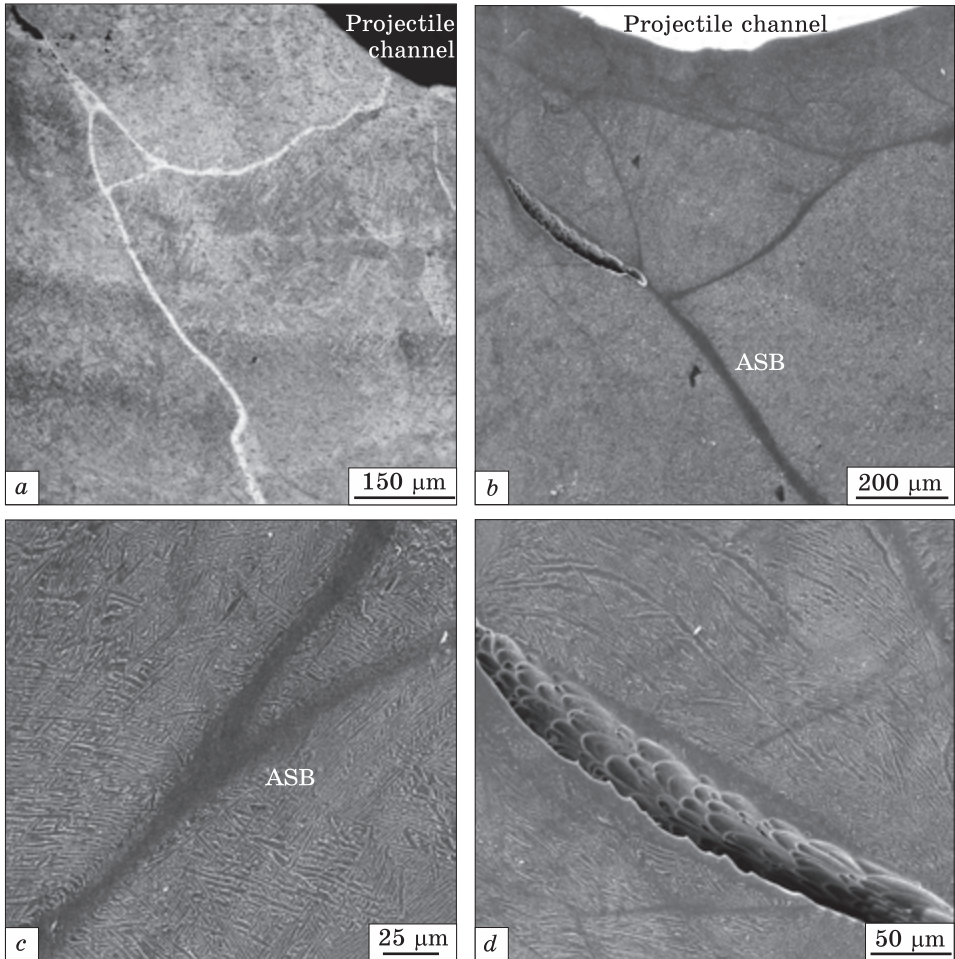


Fig. 12. General view (a, b) of severely deformed microstructure in the vicinity of projectile penetration channels, ASB (c) and crack formed within ASB (d)

ceived values of 597 J/m and 456 J/m (not completely pierced) respectively, while for 50 mm and 60 mm thick plates values of 486 J/m and 508 J/m were received. Therefore, comparison of such values allows assuming that E/d_2 ratio something above 510 J/mm is critical for piercing. As for the 7.62 mm calibre, similar dependence cannot be evaluated because no one of tested plates was pierced.

Some ambiguity in these data may also be because the bullets and their cores in the process of penetration deviated in a certain way from the original direction perpendicular to the surface (Fig. 10, b).

Typical microstructure features near projectile penetration channels are shown in Fig. 12. Ballistic impact with penetration of projectiles in

material depth is accompanied with severe high-speed deformations on the side and in front of projectile (Fig. 12, *a–b*). Localization of deformation leads to reciprocal shifting of material blocks and formation of adiabatic shear bands (ASB) with intensive material flow (Fig. 12, *a–c*). In some severely deformed locations, cracks formed within ASB and obviously deformed α phase lamellae nearby were observed (Fig. 12, *d*).

Results above demonstrated that uniform 3D printed Ti-6Al-4V alloy plates can be surely used for armour protection even against armour-piercing projectiles if their thickness is at least 30 mm. Taking in mind that stresses affecting the armour material on high-speed ballistic impact are similar to those arose on three-point flexure loading (Table 2), it was suggested that perpendicular alignment of 3D printed layers to the front surface of uniform plate is the most promising to achieve the best antiballistic protecting characteristics.

5. Layered Structures Produced with 3D Printing Approach Characterization of Initial State of Three-Layers' Materials

Above described xBeam 3D printing technology was also used for manufacturing of ternary and binary layered structures of various compositions [28–29]. The main idea for the creation of multilayered materials was to achieve the change of their microstructure and properties in a gradient manner, with strong (hard) and ductile layers alternating each other. Earlier such approach was proposed in Refs. [14, 16–19]. In our work, we realized this idea with production of layered plates (Fig. 13) in following way. Ternary layered plate (Fig. 13, *a*) was manufactured combining low strength ductile CP-Ti cast/wrought substrate as intermediate layer and 2 outer medium strength Ti-6Al-4V 3D printed layers.

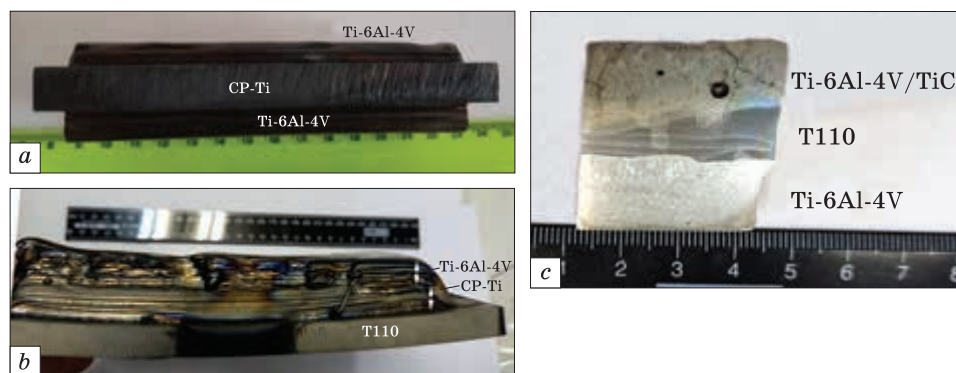


Fig. 13. Three-layered structures manufactured with 3D printing and consisting of (a) CP-Ti substrate with Ti-6Al-4V layers at both sides [28], (b) T110 substrate with CP-Ti and Ti-6Al-4V layers [29], (c) Ti-6Al-4V and MMC Ti-6Al-4V + 10% TiC printed on both sides of T110 plate (fragment)

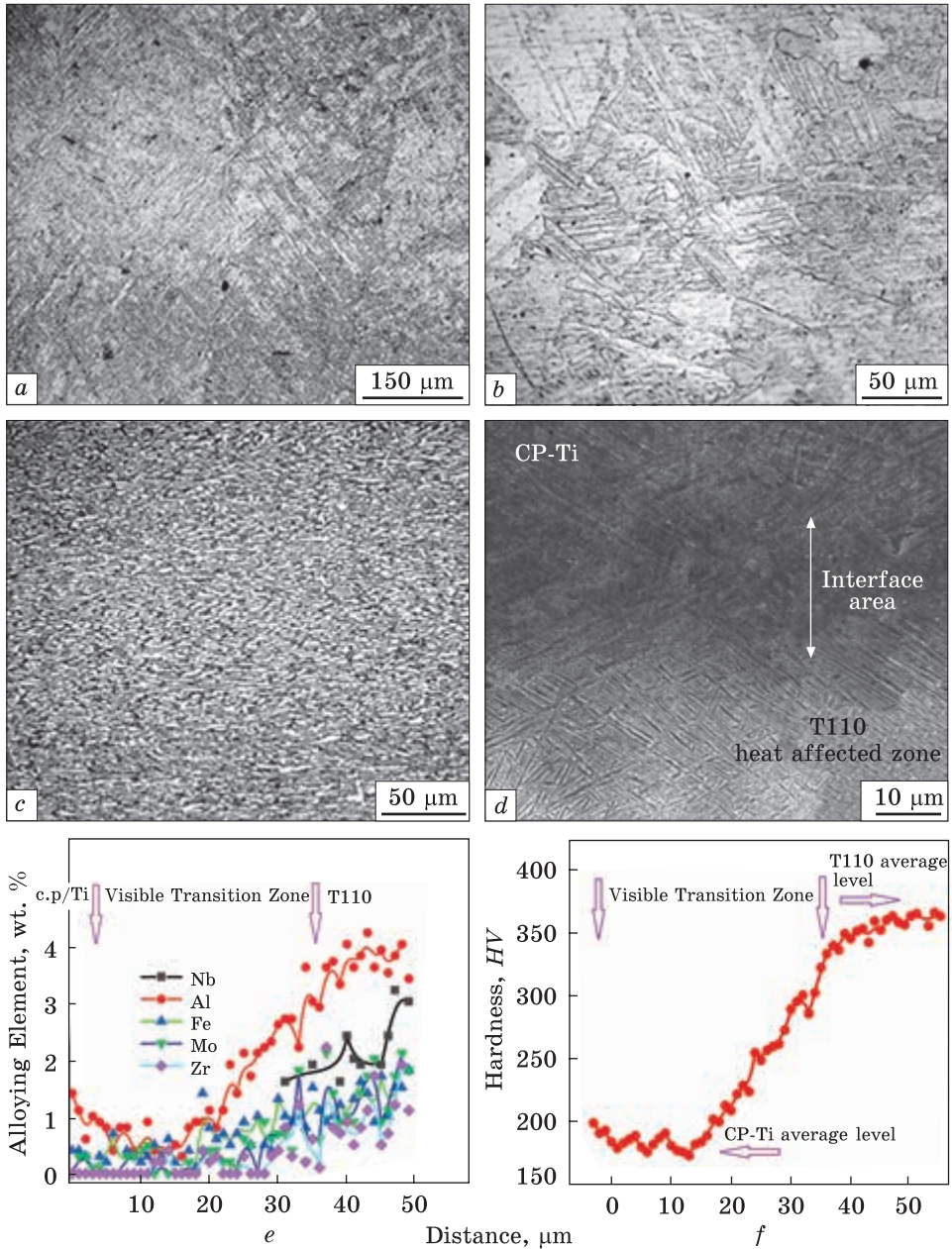


Fig. 14. Microstructures of (a) 3D printed Ti-6Al-4V, and (b) CP-Ti layers, (c) cast and wrought T110 substrate, (d) interface between CP-Ti and T110 layers. Distribution of (e) alloying elements, and (f) HV microhardness within the transition zone shown in (d) [29]

In addition, ternary material combined thermally hardenable high-strength T110 alloy (Ti-5.5Al-0.5Zr-4Nb-1.5V-1.5Mo-0.5Fe, wt.%), CP-Ti and Ti-6Al-4V was studied (Fig. 13, *b*). The cast and wrought commercial T110 plate was used as a substrate for 3D printing of CP-Ti and, then, Ti-6Al-4V layers. For the third material (Fig. 13, *c*), the high-strength cast and wrought T110 plate was joined with metal matrix composite (MMC) layer on the base of Ti-6Al-4V reinforced with particles of titanium carbide. For manufacturing of such structure, MMC of noted composition was preliminary sintered with powder metallurgy, then placed on surface of cast/wrought T110 substrate and subsequently remelted with electron beam used in xBeam technology to ensure formation of continuous MMC layer sufficiently bonded with T110. Part of opposite (back) side of T110 plate was covered with additional 3D printed Ti-6Al-4V alloy (this ternary layered part is shown in Fig. 13, *c*) while another part of T110 substrate remains binary layered (without Ti-6Al-4V) to check the useful influence of relatively ductile back layer on antiballistic protection. It should be underlined that all 3D printed multilayered structures have well-fused interfaces providing sufficient bonding between layers (Figs. 13, *c* and 14, *d*).

Quite different strength and ductile characteristics of all noted materials can be demonstrated with difference in their Vickers's hardness. Unalloyed CP-Ti demonstrates the lowest hardness of 179–188 *HV*. The hardness of 3D printed Ti-6Al-4V is noticeably higher varying within 295–377 *HV* range for different samples due to different printing regimes used for manufacturing. T110 composition belongs to high-strength titanium alloys; however, without specific strengthening heat treatment T110 plate possesses not outstanding hardness of 365 *HV*. The highest hardness is observed for Ti-6Al-4V-10% TiC MMC varying within 509–664 *HV*, the reasons of such considerable variation in hardness are not uniform redistribution of reinforcing TiC particles and harmful porosity in remelted MMC layer, which will be described below with microstructure investigations.

The typical microstructures of the individual layers are shown in Fig. 14. Both 3D printed layers (CP-Ti and Ti-6Al-4V) demonstrated coarse-grained structures with clearly visible columnar-like β grains up to 2–3 mm length, and 0.15–0.5 mm width (Fig. 14, *a, b*). Intragrain microstructure of the Ti-6Al-4V layer is characterized by fine lamellar $\alpha + \beta$ colonies (Fig. 14, *a*), while in the CP-Ti layer a mixture of α crystals of lamellar and equiaxed morphologies up to 400 μm in size is observed (Fig. 14, *b*). Contrary, cast and wrought T110 substrate has relatively fine nearly equiaxed $\alpha + \beta$ microstructure, in which α -particles are elongated in rolling direction (Fig. 14, *c*). T110 and Ti-6Al-4V materials demonstrated relatively high average hardness (365 and 377 *HV* correspondingly), such result is expected due to alloying strengthening and

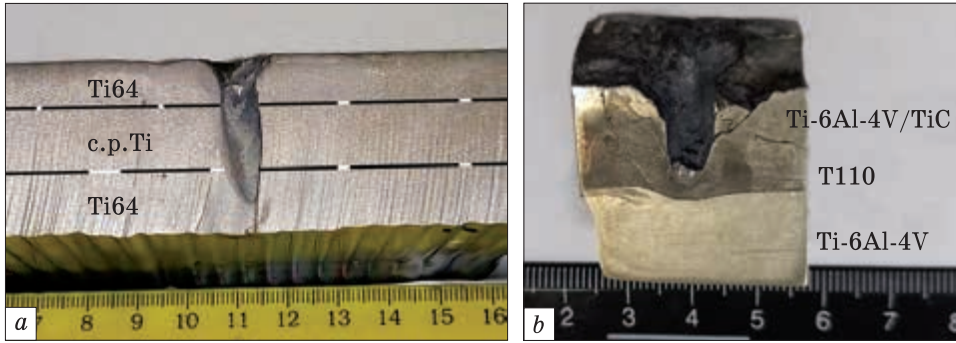


Fig. 15. Cross sections of 3-layered 3D printed materials [28] through projectile craters after ballistic testing with 7.62 mm B-32 bullets



Fig. 16. Triple Ti-6Al-4V/CP-Ti/T110 plate after ballistic tests [29]: general view from Ti-6Al-4V alloy side (a) and from T110 alloy side showing delaminated fractured area near B-32 (12.7 mm) projectile crater (b); cross sections of the plate near penetration channels of B-32 (7.62 mm) projectiles from Ti-6Al-4V alloy side (c) and T110 side (d) as well as 12.7 mm calibre from Ti-6Al-4V alloy side (e); delaminated back T110 surface near 12.7 mm bullet core stuck (f)

fine microstructure of wrought T110 plate as well as due to fine $\alpha + \beta$ intragrain microstructure of Ti-6Al-4V formed on rapid cooling during 3D printing. CP-Ti layer has the lowest average hardness of 179 HV.

Despite used 3D printing regimes ensured tight bonding and good adhesion between layers of different chemical composition without pores or other manufacturing defects at the interfaces, special attention should be paid to transition zones between the layers. Such zones were formed upon melting of both adjacent materials during 3D printing and undoubtedly have a special influence on the mechanical behaviour of a 3-layer sandwich. Fig. 14, *d* showed a typical microstructure of interface (transition zone) between 3D printed CP-Ti layer and T110 substrate. It is seen, that repeated heating and cooling during 3D building of CP-Ti layer changed microstructure within upper part of cast and wrought T110 substrate from initially globular (Fig. 14, *c*) to fine lamellar inside HAZ (heat affected zone, Fig. 14, *d*). Alloying elements distribution within corresponding transition zone between CP-Ti and T110 layers is presented in Fig. 14, *e*. From comparison of Fig. 14, *e*, *d* it is clearly seen that alloying elements, especially aluminium, penetrate quite deep into the adjacent titanium layer from the T110 substrate due to diffusion. It is expected that the presence of such a wide and smooth diffusion zone of alloying elements affects the change in mechanical characteristics. The microhardness was measured along the direction at an angle of 30° to the line showed in Fig. 14, *d* to obtain more accurate data; hardness results completely corresponded to the distribution of alloying elements (compare Fig. 14, *f*, *e*).

All layered plates were subjected to ballistic tests (Table 4, Figs. 15, 16) using 7.62 mm and 12.7 mm armour piercing B-32 projectiles and, for comparison, BZ one of 7.62 mm calibre but having lower kinetic energy than B-32. General view of projectile penetration craters in shot 3-layered materials are presented in Fig. 15. For triple plate (Fig. 15, *a*) the B-32 projectiles pierced the front Ti-6Al-4V and the intermediate CP-Ti layers and then stopped within the back Ti-6Al-4V one. The depth of penetration was 19-22 mm (Table 4, #1), while the projectile possessing some higher velocity and, hence, higher kinetic energy, was stopped with partial piercing and destruction of the back surface (Table 4, #2).

The depth of B-32 projectile crater was about of 17 mm for MMC/T110/Ti-6Al-4V plate (Fig. 15, *b*). The projectile penetrated through the MMC and T110 layers with obvious deformation of the T110/Ti-6Al-4V interface, however, did not penetrate inside back 3D printed layer (Table 4, #3). At the absence of back 3D printed Ti-6Al-4V layer, two-layered plate was nearly pierced with BZ bullet of noticeably lower kinetic energy (Table 4, #4); however, the bullet was stopped in the back surface.

Contrary to above described plates, triple Ti-6Al-4V/CP-Ti/T110 plate was tested with B-32 (7.62 mm calibre) projectiles from both opposite sides (Fig. 16, *a, b*, and Table 4, ##5, 6) to reveal possible influence of front and back layer materials on antiballistic protection. Independently on what material (Ti-6Al-4V, Fig. 16, *c* or T110, Fig. 16, *d*) was used as front side layer, B-32 projectiles of 7.62 mm calibre were stopped within back layers and the penetration depths within 21–22 mm were similar because of hardness of Ti-6Al-4V and T110 layers as well as their thickness (12 mm and 10 mm, respectively) were also comparable. The same plate was also tested from Ti-6Al-4V alloy side by B-32 projectiles of 12.7 mm calibre (Fig. 16, *e, f*) having considerably higher kinetic energies (Table 4, ##7, 8). These projectiles penetrated throughout all layers with delamination and fragmentation of backside of the plate.

Table 4. Ballistic test results of layered plates using various projectiles [29]

#	Layered plate	Total plate thickness (thickness of layers), mm	Projectile type (calibre, mm)	Kinetic energy, kJ	Penetration depth, mm	Result
1	Ti-6Al-4V/CP-Ti/	27 (8/10/9)	B-32 (7.62)	3.63	22	Projectile stopped within back layer
2	Ti-6Al-4V	27 (8/10/9)	B-32 (7.62)	3.68	27	Projectile partially pierced the plate and stuck in the back layer
3	MMC/T110/Ti-6Al-4V	30 (10/10/10)	B-32 (7.62)	3.85	17	Not pierced, stopped within T110 layer
4	MMC/T110	20 (10/10)	BZ (7.62)	2.26	16	Partially pierced; projectile stuck in back T110 plate surface
5	Ti-6Al-4V/CP-Ti/T110	34 (12/12/10)	B-32 (7.62)	3.63	21	Not pierced
6	T110/CP-Ti/Ti-6Al-4V	34 (10/12/12)	B-32 (7.62)	3.43	22	Not pierced
7	Ti-6Al-4V/CP-Ti/	34 (12/12/10)	B-32 (12.7)	16.2	34	Pierced, stopped at back surface
8	T110		B-32 (12.7)	16.8	N/A	Throughout piercing

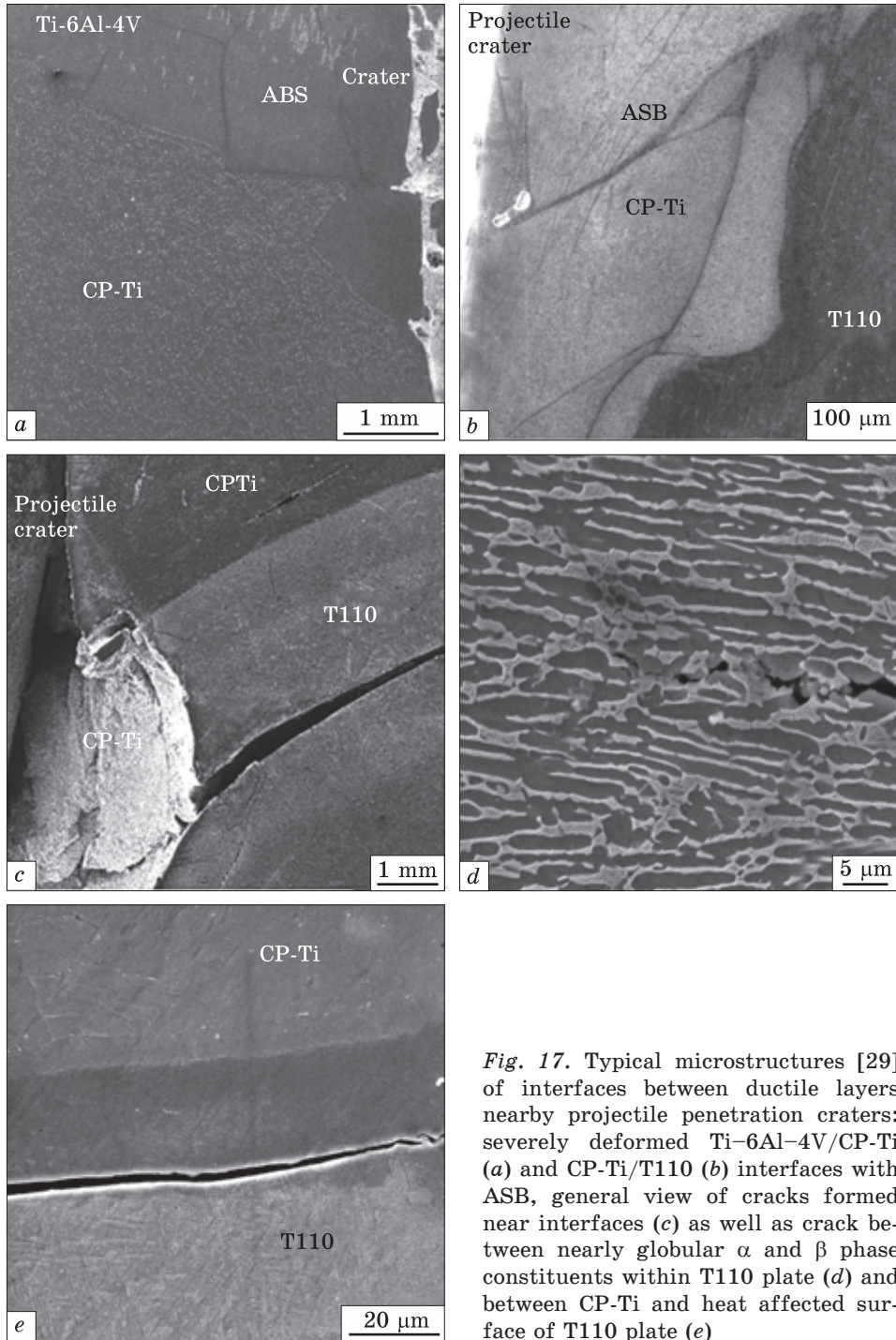


Fig. 17. Typical microstructures [29] of interfaces between ductile layers nearby projectile penetration craters: severely deformed Ti-6Al-4V/CP-Ti (a) and CP-Ti/T110 (b) interfaces with ASB, general view of cracks formed near interfaces (c) as well as crack between nearly globular α and β phase constituents within T110 plate (d) and between CP-Ti and heat affected surface of T110 plate (e)

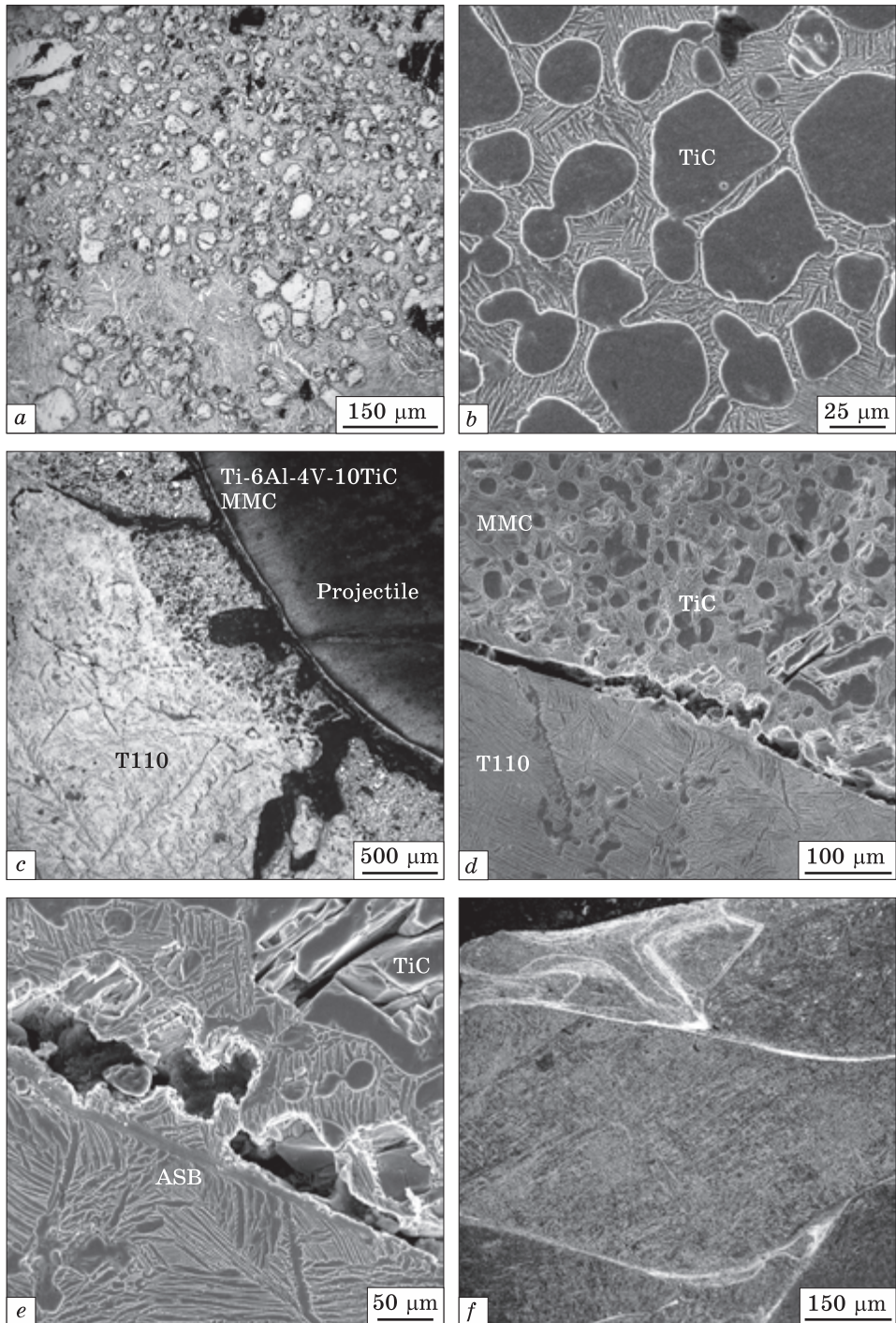


Fig. 18. Distinctive microstructure features of ternary Ti-6Al-4V-10%TiC MMC/T110/Ti-6Al-4V plate: (a) non-uniform redistribution of TiC particles and pores in remelted MMC layer, (b) TiC particles in lamellar Ti-6Al-4V matrix within MMC layer; (c) general view of damaged MMC and T110 layers near projectile crater, (d) crack at the interface between MMC and T110 layers, (e) crack, ASB and crushed TiC particles in severely deformed area between layers, (f) severely deformed area with ASB in T110 layer near the bottom of projectile crater

The role of individual material layers in retardation of projectiles became understanding from the analysis of the most characteristic microstructure features nearby projectile craters (Figs. 17, 18). For layered samples consisted of Ti-6Al-4V, CP-Ti and T110 alloys (Fig. 13, *a, b*), which are relatively ductile materials, severe deformation within individual layers and at the interfaces between layers was observed (Fig. 17) with ASB formation and shifting of interfaces (Fig. 17, *a, b*). Also, a number of cracks was observed near interfaces (Fig. 17, *c*) due to different strength and ductile characteristics of adjacent materials, and, hence, different their deformation ability. For example, cracks were formed within nearly globular microstructure of cast/wrought T110 plate at interfaces between α and β phase constituents (Fig. 17, *d*). This type of T110 microstructure was transformed into fine lamellar one (Fig. 17, *e*) in heat affected surface area on 3D printing of CP-Ti and cracks also formed directly at the interface between relatively coarse α structure of CP-Ti layer and fine lamellar one of T110 heat affected surface (Fig. 17, *e*). Other microstructure features of individual deformed alloy layers were quite similar to those earlier observed for individual 3D printed Ti-6Al-4V material (Fig. 12).

As for layered plate with Ti-6Al-4V-10% TiC MMC at the surface (Fig. 13, *c*), which is markedly harder and rather brittle material, there are some other microstructure features (Fig. 18). Remelted MMC surface layer was characterized with noticeable inhomogeneity in size and space distribution of reinforcing TiC particles (Fig. 18, *a*) as well as porosity in Ti-6Al-4V matrix having fine lamellar structure (Fig. 18, *b*) which was formed on relatively fast cooling after remelting. The maximal size of TiC particles observed after remelting was unexpectedly large (up to 400 μm) due to possible coagulation, thus, being obviously undesirable to achieve the outstanding balance of hardness, strength and ductile characteristics. Such microstructure inhomogeneity and porosity resulted in considerable variation in hardness within MMC layer. The projectile severely damaged front MMC and next T110 layers with formation of number of cracks (Fig. 18, *c*), which observed at interface between layers (Fig. 18, *d*), in T110 layer, and, especially, within relatively brittle MMC layer. Despite small individual TiC particles were found in upper part of T110 substrate (Fig. 18, *d, e*), which was also melted during surface heating with electron beam, MMC and T110 layers demonstrated noticeably different abilities for deformation. Crushed TiC particles, mainly those of larger sizes, were the only visible traces of deformation in MMC matrix (Fig. 18, *e*), while a number of ASBs and bended α phase lamellae nearby (Fig. 18, *e, f*) were observed in ductile T110 alloy. Such difference in deformation ability of hardened MMC and adjacent ductile T110 alloy layers resulted in cracks formation along the interface (Fig. 18, *c, d, e*). As for back Ti-6Al-4V layer, it was not noticeably deformed.

For better understanding of the influence of each layer, interfaces between them and reciprocal arrangement of different materials in layered structures on antiballistic protection characteristics, three points flexure testing were performed using binary layered samples (Table 5) to imitate loading conditions similar to those arose on projectile impact. The loading was applied to central area of upper layer, thus, upper layer was subjected to compression stresses on bending while bottom one — to tensile stresses. The testing results (Table 5) once more confirmed that binary-layered materials were more enduring against flexure deformation possessing higher strain before fracture if hardened front layer and more ductile back layer were used (Table 5, ##2, 4). Binary samples which includes ductile CP-Ti layer as back material (Table 5) allow to achieve obviously better flexure strain (20–24%) but lower strength (1271–1445 MPa) than uniform Ti–6Al–4V alloy (Table 2). Opposite arrangement of layers (Table 5, ##1, 3) resulted in higher strength characteristics but lower strain parameters. However, all tested binary layered materials (Table 5) demonstrated lower 3-point flexure strength than that for uniform Ti–6Al–4V alloy (Table 2); this result is in agreement with deeper projectile penetration in ternary-layered plates due to presence of soft CP-Ti layer.

From the analysis of Tables 3 and 4 results taking B-32 projectiles of the same 7.62 mm calibre and, hence, similar kinetic energies, the following suggestions can be made. Due to the presence of soft CP-Ti layer in ternary-layered materials, they demonstrated some deeper penetration of projectiles (21–22 mm) than in uniform Ti–6Al–4V alloy (17–20.5 mm). On another hand, presence of ductile intermediate or back layer is useful because of ductile layer eliminates throughout piercing with brittle fracture of either entire plate or their back surface (like those shown in Figs. 10, *a*, and 16, *b*, *e*) on ballistic impact. At the same time, hard front layer like Ti–6Al–4V–10TiC MMC promotes better retardation of projectiles and, hence, lower penetration depth (17 mm), however, intensive cracking and destruction of hard and brittle MMC front surface (Fig. 15, *b*) was observed on ballistic impact, this fact restricts using of MMC alone for sustainable antiballistic protection. Thus, once more was confirmed that the improved and sustainable

Table 5. Three-point flexure characteristics of binary layered samples [29]

#	Upper/bottom layer	Flexure stress, MPa	Flexure strain, %
1	CP-Ti/Ti–6Al–4V	1552	14.1
2	Ti–6Al–4V/CP-Ti	1445	20.1
3	CP-Ti/T110	1822	18.4
4	T110/CP-Ti	1271	23.9

antiballistic protection with reduction of total thickness of armour plates can be achieved with combination of front hard and back (inner) ductile layers. Hard front layer like MMC or high-strength titanium alloy need more energy for deformation and crushing of reinforcing particles (TiC, TiB), thus, spends significant part of projectile kinetic energy. Ductile back layers with improved fracture toughness parameters (e.g., within 4–40 MPa·m^{1/2} for titanium alloys [1]) needs high energy for crack propagation, promotes retardation of this harmful process and makes impossible instant brittle failure. Moreover, it is believed, important is the role of interface boundaries in multilayered structures, which provide reflection and redirection of elastic impact waves along the armour plate, thus, promoting better dissipation of kinetic energy of projectiles and their retardation.

6. Comparison with Other Armour Materials

The conclusion about the effectiveness of 3D printed products can only be made by comparing the results obtained with similar ballistic test data for other materials. It was shown in our previous publications, that titanium alloys Ti–6Al–4V and T110 demonstrated more attractive mechanical behaviour on dynamic loading testing than high strength armour steels like ARMOX600T and others, if specific weight of these materials is considered [28, 29]. Similar advantages were found when these alloys were ballistically tested with some kind of ammunition [19]. Fig. 19 presents a comparative dependence of V50 characteristic versus thickness of tested plates for 3D printed Ti–6Al–4V material described in part 4 and single composition (uniform) titanium alloy plates [26]. It is clearly seen that obtained by J. Fanning dependence is linear, while main results obtained for rolled Ti–6Al–4V plates are on that line. Obtained in present work values of penetration depth also are rather close to this dependence. However, present data correspond to not pierced situation, while V50 parameter means projectile velocity at which probability of piercing/not piercing is 50/50. Therefore, it is possible to conclude that real V50 values for 3D printed plates are essentially higher than shown in Fig. 19 with crosses, and such material is even better for ballistic resistance than conventional cast and wrought plates of the same composition. It can be assumed that such superiority of the 3D material is due to its layered microstructure and specific crystallographic texture (see Section 3).

Efficiency of different titanium-based materials, including layered ones, on ballistic tests is compared in Fig. 20. Uniform 3D printed Ti–6Al–4V plates demonstrated comparable penetration depth of B32 bullets (designated as X) with those for all layered materials. Corresponding points on the diagram are located mainly on the left side of the

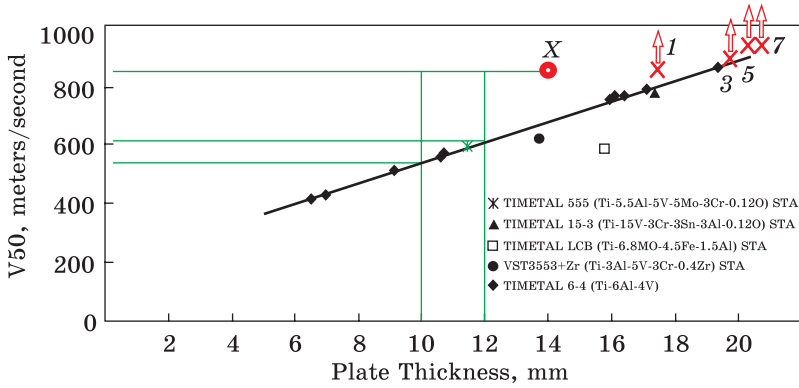


Fig. 19. Dependence of V50 critical velocities of 7.62×52 mm AP ammunition on thickness of Titanium plates (mainly made of Ti-6Al-4V) obtained in Refs. [30, 31] (black symbols and line). Point X — V50 for 14 mm thick Ti-6Al-4V rolled plate obtained in Ref. [32]. Red crosses indicate penetration depth (without piercing) by similar B32 bullets. Numbers correspond positions in Table 3; arrows mean that real V50 values are higher

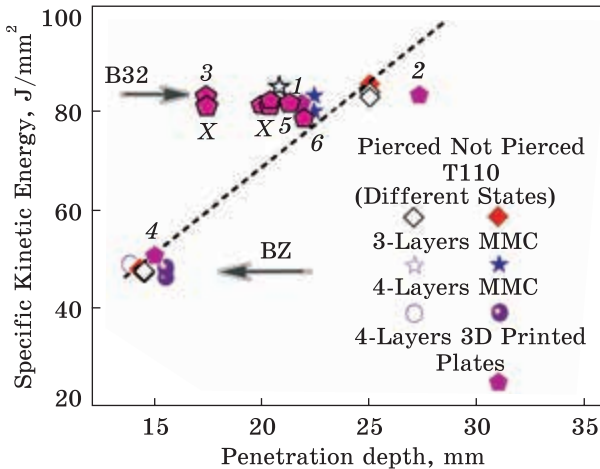


Fig. 20. Comparison of ballistic resistance of different Ti-based materials as penetration depth of BZ and B32 bullets (both of 7.62 mm calibre). Numbers near pentagons correspond to pp. in Table 4; symbols with X show position of test results of 3D printed Ti-6Al-4V from Table 3. Data for T110 alloy and layered MMC were taken from Refs. [33, 28], respectively

general (dotted) line separating pierced and not pierced materials. The maximum penetration depth of B32 bullet was observed for the 3-layer material with the intermediate softest CP-Ti layer (shown as pentagon #2, Fig. 20 and p. #2 in Table 4). However, the same layered material demonstrated noticeably reduced penetration depth for bullet having bit lower kinetic energy (#1, Fig. 20 and Table 4), suggesting some inhomogeneity of local protecting characteristics. For 3-layer material consisting of T110, CP-Ti and Ti-6Al-4V ballistic impacts with opposite sides (#5 and #6 in Fig. 20 and in Table 4) resulted in nearly similar penetration depth (20–21 mm) due to ductile condition of T110 alloy

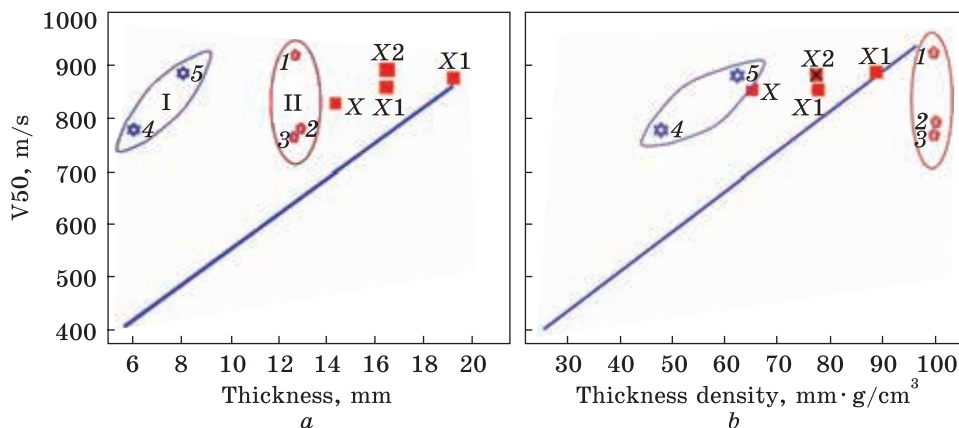


Fig. 21. Comparison of dependence of V50 values vs. thickness of steel plates (points #1–5) and titanium materials (points X–X2) estimated in ballistic tests with 7.62 AP ammunition: (a) in absolute thickness values, and (b) taking into account specific weight of materials. Blue line was obtained in Refs. [30, 31] with a wide range of commercial titanium alloys. Data for regions I, II were taken from Refs. [34, 35], respectively. Point X — V50 for 14 mm thick Ti–6Al–4V rolled plate obtained [31], points X1 — 3D printed uniform Ti–6Al–4V, X2 — layered 3D printed material

layer which strength is close to Ti–6Al–4V one. Finally, the lowest penetration depth (17 mm), and, hence, the greatest ballistic resistance, was shown by a 3-layer material in which a front (surface) layer was hardened with carbide particles (#3 in Fig. 20 and Table 4). When this material was tested with BZ bullet (#4 in Fig. 20 and Table 4), the penetration depth was even lower.

It is quite important from practical point of view to compare tested titanium materials with special armour steels. Such a comparison is made in Fig. 21. Fig. 21, a illustrates comparison of V50 values of several steels from ARMOX family with general dependence obtained earlier for a wide range of commercial titanium alloys [31] in nominal values of plate thicknesses. It is clearly seen that results for ARMOX steels are localized in two areas designated as (I) and (II). First of them corresponds to tests performed at 30° obliquity, while the second one was strictly perpendicular shooting of targets, like all tests performed for titanium-based materials. Our own data for uniform 3D printed Ti–6Al–4V alloy (points X1) and for layered material with MMC front layer (X2 one) are between steel results and general linear dependence for commercial titanium alloys (Fig. 21, a). So, in such coordinates, the superiority of steels over titanium alloys is obvious, demonstrating lower thickness of steel material necessary for sustainable protection against ballistic impacts. However, if difference in the specific weight of steels and titanium alloys will be taken into account (Fig. 21, b) the situation

has fundamentally changed. Namely, the plates shot at an angle of 90° (region (II)) are located on the right side of the common line for titanium alloys, *i.e.*, have less durability. From the left side of the line is the region (I) only, corresponding to firing at 30° angle which significantly weakened the test conditions. In such coordinates 3D printed Ti-6Al-4V alloy (points X1) and the multilayer structure with hard MMC front layer (point X2) obviously demonstrate advantage over steels as armour protecting materials.

Thus, the data presented unequivocally show that titanium-based 3D printed materials have high ballistic resistance characteristics, especially when they include high-strength layers, in particular those reinforced with hard particles. Generally, above described results showed the promising potential of 3D printing technologies, xBeam 3D Metal Printing as an example, for manufacturing of titanium-based multilayer armour materials with reduced thickness and weight, at the same time, sufficient protection characteristics (see also Refs. [36, 37] and references therein).

7. Conclusions

The potential of xBeam 3D Metal Printing approach for additive manufacturing of uniform and multilayered titanium-based armour materials was investigated using comprehensive microstructure studies, mechanical and ballistic testing.

Optimization of 3D printing parameters ensures formation of desirable uniformity of grain structure with sufficient isotropy of mechanical characteristics. Taking the most widely used Ti-6Al-4V titanium composition as an example, strength and ductile characteristics, which met standard requirements, were achieved. Such a material can have a wide practical application; however, the attention should be paid to the features of the microstructure anisotropy and crystallographic texture, which have noticeable potential to affect mechanical characteristics.

Multilayered plates consisted of titanium alloys as well as titanium-based metal matrix composites ensure a unique set of hardness, strength and ductile properties owing to combination of materials possessing quite different mechanical characteristics. Multilayered plates can be successfully manufactured using 3D metal printing and electron beam remelting technologies.

Peculiarities of material deformation and structure evolution under high-energy ballistic impact were investigated. Obtained results are useful for development of general recommendations for reduction of thickness and weight of titanium-based armour by creation of multilayered structures.

REFERENCES

1. G. Lutjering and J.C. Williams, *Titanium*, 2nd ed. (Berlin, Heidelberg: Springer: 2007);
<https://doi.org/10.1007/978-3-540-73036-1>
2. W.E. Frazier, *J. Mater. Eng. Perform.*, **23**, No. 6: 1917 (2014);
<https://doi.org/10.1007/s11665-014-0958-z>
3. T. Wohlers, I. Campbell, T. Caffrey, O. Diegel, and J. Kowen, *Wohlers Report 2018: 3D Printing and Additive Manufacturing State of the Industry : Annual Worldwide Progress Report* (Wohlers Associates: 2018).
4. B. Gadagi and R. Lekurwale, *Materials Today: Proceedings*, **45**: 277 (2021);
<https://doi.org/10.1016/j.matpr.2020.10.436>
5. S. Liu and Y. C. Shin, *Materials & Design*, **164**: 107552 (2019);
<https://doi.org/10.1016/j.matdes.2018.107552>
6. M. Saunders, Boosting AM adoption — the next phase of market growth (LinkedIn: May 29, 2018).
7. C. Decaillet, Additive manufacturing — challenges to face, *Int. Conf. Titanium 2017* (October 8–11, 2017, Florida, USA).
8. F. Pixner, F. Warchomichka, P. Peter, A. Steuwer, M.H. Colliander, R. Pederson, and N. Enzinger, *Materials*, **13**, No. 15: 3310 (2020);
<https://doi.org/10.3390/ma13153310>
9. B. Wysocky, P. Maj, R. Sitek, J. Buhagiar, K.J. Kurzydłowski, and W. Świążkowski, *Applied Sciences*, **7**: 657 (2017);
<https://doi.org/10.3390/app7070657>
10. A.H. Chern, P. Nandwana, T. Yuan, M.M. Kirka, R.R. Dehoff, P.K. Liaw, and C.E. Duty, *International Journal of Fatigue*, **199**: 173 (2019);
<https://doi.org/10.1016/j.ijfatigue.2018.09.022>
11. M. Peters, J. Kumpfert, C.H. Ward, and C. Leyens, *Advanced Engineering Materials*, **5**, No. 6: 419 (2003);
<https://doi.org/10.1002/adem.200310095>
12. T.L. Jones, K. Kondoh, T. Mimoto, N. Nakanishi, and J. Umeda, *Key Engineering Materials*, **551**: 118 (2013);
<https://doi.org/10.4028/www.scientific.net/KEM.551.118>
13. J.S. Montgomery and M.G.H. Wells, *JOM*, **4** : 29-32 (2001);
<https://doi.org/10.1007/s11837-001-0144-2>
14. J.A. Zukas and D.R. Scheffler, *International Journal of Solids and Structures*, **38**: 3321 (2001);
[https://doi.org/10.1016/S0020-7683\(00\)00260-2](https://doi.org/10.1016/S0020-7683(00)00260-2)
15. N.K. Gupta and V. Madlu, *International Journal of Impact Engineering*, **19**: 395 (1997);
[https://doi.org/10.1016/S0734-743X\(97\)00001-8](https://doi.org/10.1016/S0734-743X(97)00001-8)
16. J.K. Lee, *Analysis of Multi-Layered Materials under High Velocity Impact Using CTH* (Thesis, Master of Science in Aeronautical Engineering: 2008);
<https://scholar.ait.edu/etd/2685>
17. O.M. Ivasishin, P.E. Markovsky, D.G. Savvakina, O.O. Stasiuk, and S.V. Prikhodko, *Journal of Materials Processing Technology*, **269**: 172 (2019);
<https://doi.org/10.1016/j.jmatprotec.2019.02.006>
18. P.E. Markovsky, D.G. Savvakina, O.M. Ivasishin, V.I. Bondarchuk, and S.V. Prikhodko, *Journal of Materials Engineering and Performance*, **28**: 5772 (2019);
<https://doi.org/10.1007/s11665-019-04263-0>
19. O.M. Ivasishin, P.E. Markovsky, D.G. Savvakina, O.O. Stasiuk, V.A. Golub, V.I. Mir-

- nenko, S.H. Sedov, V.A. Kurban, and S.L. Antonyuk, Microstructure and properties of titanium-based materials promising for antiballistic protection, *Progress in Physics of Metals*, **20**, No. 2: 285 (2019);
<https://doi.org/10.15407/ufm.20.02.285>
20. D. Kovalchuk and O. Ivasishin, Profile electron beam 3D metal printing, *Additive Manufacturing for the Aerospace Industry* (Eds. F. Froes and R. Boyer) (Elsevier: 2019), p. 213;
<https://doi.org/10.1016/B978-0-12-814062-8.00012-1>
21. D. Kovalchuk, V. Melnyk, I. Melnyk, and B. Tugai, *Journal of Elektrotechnica & Elektronika*, Nos. 5–6: 36 (2016).
22. D.V. Kovalchuk, V.I. Melnik, I.V. Melnik, and B.A. Tugai (Review, in Russian), *Automatic Welding*, No. 12: 26 (2017);
<https://doi.org/10.15407/as2017.12.03>
23. D. Kovalchuk, V. Melnyk, I. Melnyk, and B. Tugai, *Journal of Elektrotechnica & Elektronika*, **53**, Nos. 3–4: 60 (2018).
24. O.V. Makhnenko, A.S. Milenin, E.A. Velikoivanenko, N.I. Pivtorak, and D.V. Kovalchuk, *The Paton Welding Journal*, **3**: 7 (2017);
<https://doi.org/10.15407/tpwj2017.03.02>
25. D. Kovalchuk, G. Grygorenko, A. Tunik, L. Adeeva, S. Grygorenko, and S. Stepanyuk, *Electrometallurgy Today*, **133**, No. 4: 62 (2018);
<https://doi.org/10.15407/sem2018.04.05>
26. D. Kovalchuk, V. Melnyk, I. Melnyk, D. Savvakin, O. Dekhtyar, O. Stasiuk, and P. Markovsky, *Journal of Materials Engineering and Performance*, **30**, 7: 5307 (2022);
<https://doi.org/10.1007/s11665-021-05770-9>
27. D. Kovalchuk, O. Ivasishin, and D. Savvakin, *MATEC Web of Conf.*, **321**: 03014 (2020);
<https://doi.org/10.1051/mateconf/202032103014>
28. P.E. Markovsky, D. Savvakin, O.O. Stasiuk, S.G. Siedov, V.A. Golub, D.V. Kovalchuk, and S.V. Prikhodko, *Metallofizika i Noveishie Tekhnologii*, **43**, No. 12: 1573 (2021);
<https://doi.org/10.15407/mfint.43.12.1573>
29. P.E. Markovsky, O.M. Ivasishin, D.G. Savvakin, O.O. Stasiuk, V.I. Bondarchuk, D.V. Oryshych, D.V. Kovalchuk, S.H. Sedov, V.A. Golub, and V.V. Buznytskyi, *Metallofizika i Noveishie Tekhnologii*, **44**, No. 10: 1361 (2022);
<https://doi.org/10.15407/mfint.44.10.1361>
30. J. Fanning, *J. Mater. Eng. Perform.*, **14**: 686 (2005);
<https://doi.org/10.1361/105994905X75457>
31. J. Fanning, *Proceedings of the 11th World Conference on Titanium* (3–7 June 2007, Kyoto, Japan) (The Japan Institute of Metals Publish: 2007], Vol. 1, p. 487.
32. J. Janiszewski, B. Fikus, and P.E. Markovsky (Military University of Technology, Warsaw, Poland: 2022) (unpublished work).
33. P.E. Markovsky, J. Janiszewski, V.I. Bondarchuk, O.O. Stasyuk, K. Cieplak, and O.P. Karasevska, *Metallography, Microstructure, and Analysis*, **10**: 839 (2021);
<https://doi.org/10.1007/s13632-021-00797-9>
34. D.D. Showalter, W.A. Gooch, M.S. Burkins, and R. Stockman Koch, Ballistic testing of SSAB ultra-high-hardness steel for armor applications (Army Research Laboratory, ARL-TR-4632: 2008);
<https://apps.dtic.mil/sti/pdfs/ADA493654.pdf>

35. W.A. Gooch, M.S. Burkins, R. Squillaciotti, R.-M. Stockman Koch, H. Oscarsson, and C. Nash, Ballistic testing of Swedish steel ARMOX® plate for U.S. armor application (21st International Symposium on Ballistics, 19–23 April 2004, Adelaide, South Australia).
36. M.O. Vasylyev, B.M. Mordyuk, and S.M. Voloshko, *Progress in Physics of Metals*, **24**, No. 1: 5 (2023);
<https://doi.org/10.15407/ufm.24.01.005>
37. M.O. Vasylyev, B.M. Mordyuk, and S.M. Voloshko, *Progress in Physics of Metals*, **24**, No. 1: 38 (2023);
<https://doi.org/10.15407/ufm.24.01.038>

Received 11.01.2023;
in final version, 23.01.2023

*О.М. Івасишин¹, Д.В. Ковальчук², П.Є. Марковський¹, Д.Г. Саввакін¹,
О.О. Стасюк¹, В.І. Бондарчук¹, Д.В. Оришич¹, С.Г. Седов³, В.А. Голуб³*

¹ Інститут металознавства ім. Г.В. Курдюмова НАН України,
бульв. Академіка Вернадського 36, 03142 Київ, Україна

² ПРАТ «НВО «ЧЕРВОНА ХВИЛЯ»,
вул. Дубровицька, 28, 04114 Київ, Україна

³ Національний університет оборони України імені Івана Черняховського,
Повітрофлотський проспект, 28, 03049 Київ, Україна

АДИТИВНЕ ВИРОБНИЦТВО МАТЕРІАЛІВ НА ОСНОВІ ТИТАНУ МЕТОДОМ 3D-ДРУКУ З ВИКОРИСТАННЯМ ЕЛЕКТРОННО-ПРОМЕНЕВОГО ТОПЛЕННЯ ДРОТУ: ОСОБЛИВОСТІ, ПЕРЕВАГИ ТА ПЕРСПЕКТИВИ

Потенціал адитивних технологій, а саме, технології xBeam 3D Metal Printing було продемонстровано для виготовлення однорідного стопу Ti-6Al-4V (Ti-6-4, мас. %), а також шаруватих структур на основі титану з механічними властивостями, достатніми для широкого практичного застосування. Основними відмінними рисами цього процесу є використання дроту із титанового сплаву як вихідного матеріалу й електронного променя кінчної форми для нагріву та топлення дроту. Стоп Ti-6-4, одержаний 3D-друком за розробленою «стратегією зсуву», відповідає вимогам щодо механічних характеристик відповідних литих і кованих виробів, якщо особливості мікроструктури, анізотропії матеріалу та кристалографічної текстури контролюються належним вибором параметрів процесу. Описано виробництво багатшарових структур, де комбінуються шари різних титанових матеріалів, а саме, технічно чистого титану (CP-Ti), Ti-6-4, високоміцного стопу T110, а також металоматричних композитів (ММС) на основі Ti-6-4, зміцнених частинками TiC. Проаналізовано мікроструктурні особливості та механічні властивості всіх 3D-друкованих матеріалів. Проведено балістичні випробування вказаних матеріалів різними кулями. Описані результати показали багатообіцяючий потенціал технологій 3D-друку, наприклад xBeam 3D Metal Printing, для виготовлення багатшарових броньових матеріалів на основі титану зі зменшеною товщиною та вагою, і, в той же час, достатніми захисними характеристиками.

Ключові слова: титанові стопи, 3D-друк, мікроструктура, багатшаровий матеріал, механічні властивості, антибалістичний захист.